The International Journal of Advanced Manufacturing Technology (2018) 99:1405–1425
https://doi.org/10.1007/s00170-018-2525-5

ORIGINAL ARTICLE

Projection welding of nuts involving the use of electromechanical and pneumatic electrode force

Zygmunt Mikno [1]

Received: 14 April 2018 / Accepted: 30 July 2018 / Published online: 22 August 2018

Abstract

The projection welding of nuts performed using the pneumatic (electrode) force system (PFS) was subjected to thorough numerical and experimental analysis, enabling the identification of the window of welding parameters taking into consideration boundary conditions including expulsion, torsional strength and the deformation of the nut thread. The welding process was subjected to optimisation involving the use of a new, i.e. electromechanical (electrode) force system (EFS). The optimisation-related approach involved the reduction of welding current and the extension of a welding current flow time in comparison with those obtained when using the pneumatic force system. It was assumed that the acceptance criterion would be the breaking torque not lower than that obtained under the most favourable welding conditions performed using the PFS. The research work involved comparative numerical calculations (performed using the SORPAS software) in relation to both, i.e. the PFS and EFS. The technological welding tests were performed using inverter welding machines (1 kHz) provided with various (electrode) force systems. The research work also included metallographic tests, hardness measurements and torsional strength tests. As a result of the application of EFS and a special innovative *hybrid* algorithm for controlling the electrode clamps, a wider and higher weld core was obtained. The depth of "*penetration*" into the sheet was greater. As a result, the welded joint has a higher resistance (by 30%). Technological welding tests for the new EFS system were carried out for a 25% lower welding current compared with PFS. Despite the lower welding current for EFS, the welding energy is slightly lower but the welding quality for EPS is significantly higher.

Keywords FEM · Electromechanical force system · Resistance welding · Projection welding

1 Introduction

Technologically advanced car bodies contain approximately 300 welded and clamped fasteners, e.g. bolts, nuts and pins, to which key safety features including seat belts, steering columns or the earthing of electric circuits are fastened [1]. The quality of welded joints is of critical importance as regards the safety and reliability of end products.

However, the projection welding of nuts is characterised by numerous disadvantages and limitations, including (i) narrow window of welding parameters, (ii) lack of repeatability, (iii) sensitivity to the lack of tolerance in relation to the height of the projection and the hardness of the material subjected to welding, (iv) initial impact of electrodes, (v) insufficient dynamics of the force system, (vi) risk of expulsion and (vii) lack of ability to modulate the electrode pressure force during the current flow. The foregoing disadvantages lead to deteriorated quality.

The above-named disadvantages could be primarily linked to the use of the pneumatic force system (PFS), characterised by significant mechanical inertia and the impossibility to control force, particularly during the welding current flow [2]. The process of welding is also significantly affected by the areas of projections during welding [3] and, in particular, the stability of welding power density in relation to the present area of contact between elements being welded [4].

A characteristic of projection welding, for PFS, is the fact that the joint is obtained in the solid state. The foregoing results from the fact that the molten material is pushed outside the welding area by excessive electrode force. This, in turn, leads to a significant increase in the area of contact between materials being welded (nut projection and sheet) and a rapid

✉ Zygmunt Mikno
zygmunt.mikno@is.gliwice.pl

[1] Welding Institute from Poland, Bl. Czeslawa 16-18, 44-100 Gliwice, Poland

decrease in current density. As a result, the melting of the material is significantly restricted (nearly stopped) as early as at the initial stage of current flow. The zone of the molten material, if any, is extremely narrow.

An alternative solution could involve the use of the electromechanical force system (EFS). The authors emphasise the growing popularity of such an electrode force system [5], the possibility of extending the window of technological parameters [6], the possibility of adjusting the force of electrode [7, 8], the extended service life of electrodes [9] and the possibility of eliminating the dynamic impact of electrodes against the material being welded (during the initial squeeze) [10, 11]. Work [11] enumerates other advantages related to the use of the EFS such as (i) faster handling of a servo welding gun in the operating space, (ii) higher electrode force repeatability, (iii) reduced noise, (iv) shorter welding time and (v) smaller movement (displacement) when closing and opening electrodes, extending the service life of welding machine mechanisms.

However, the application only of the EFS is insufficient. The essence of the improvement of the resistance welding process is the possibility of changing force during the welding process, especially during the current flow. Improving the weld quality by applying a variable force is described in [12–15]. This control method can be called control according to the *force control algorithm*. The control method for EFS is better than that for PFS. However, it is characterised by a delay in obtaining a preset force value by approximately 50–70 ms. This delay depends on the type of servo motor and mechanical transmission.

There is another, more effective, method of controlling the pressure force of the electrodes, i.e. controlling the movement of the electrodes. The delay mentioned above, in this case, is very small (about 1 ms), and this is a very important advantage of the new control method. The authors of the publication [16, 17] applied EFS and a special hybrid algorithm of control according to the *movement of electrode*. The authors describe a new control system and the results of its operation, particularly visible in projection welding. This is an innovative approach to controlling the electrode movement. In the available literature no information about a similar solution was encountered.

The aim of the new solution is to improve the quality of welded joints, in particular to projection welding. The new control method of electrode, described for projection welding, significantly changes the usual views in terms of resistance welding and significantly influences the development of research in this field.

The article is part of the research in which the welding process is analysed for the use of a variable force during the current flow. The new control method is implemented by means of EFS and a special hybrid algorithm.

2 Methodology of numerical and experimental tests

The process of the projection welding of nuts involving the use of the PFS was subjected to thorough numerical and experimental analysis. Afterwards, the process was optimised by involving the EFS. The adopted optimisation approach involved the reduction of welding current and the extension of its flow time. It was assumed that the acceptance criterion would be a torque (M_B) not lower than that obtained in relation to the most favourable conditions of welding performed using the PFS.

The nut used in the tests is presented in Fig. 1. The dimensions of the nut are detailed in Table 1.

2.1 FEM calculations

The numerical calculations were performed using the SORPAS software, i.e. the 2D and 3D models, respectively [18, 19]. The SORPAS software is dedicated to the process of resistance welding and enables the performance of conjugated electric, thermo-metallurgical and mechanical calculations. The SORPAS software makes it possible to implement an electrode displacement control algorithm, i.e. one of algorithms related to the control of a servomotor applied in the EFS used in the experimental tests [20].

2.2 Numerical model

The numerical model concerned with the welding of a nut to the sheet is presented in Fig. 2 Process-related calculations were performed using both the 2D and the 3D model. The 2D model was used as only this model featured certain functions important in terms of performed analysis, e.g. power density distribution.

The software programme enables the performance of related analyses, including coupled electro-thermo-mechanical-metallurgical analyses. The above-named software features a module including the effect of a new force and a precise electrode movement solution, i.e. based on the EFS.

The 3D model was composed of 4379 eight-node hexahedral and six-node prismatic elements. Mentioned above elements provide three degrees of freedom (DOF) in each node for the velocity components of plastic flow in the mechanical model and one DOF for modelling the scalar fields of temperature and one DOF for electrical potential. The solution was performed using explicit time integration scheme [21].

The numerical calculations involved the analysis of (i) waveforms of dynamic resistance and momentary power, (ii) energy supplied to the weld, (iii) width, height and volume of the molten weld nugget, (iv) displacement of electrodes and (v) expulsion. The primary objective was to determine the

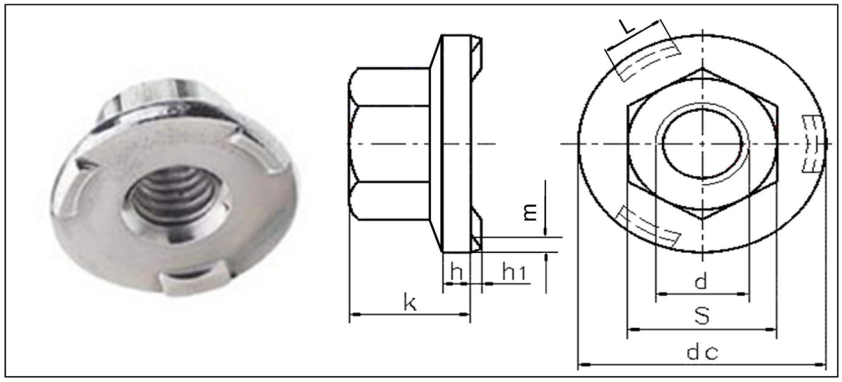

Fig. 1 Nut with three full projections: **a** nut and **b** scheme with designated dimensions (Table 1)

most favourable space distribution of welding power enabling the obtainment of the desirable weld nugget shape including deeper penetration in the sheet and a greater width of the weld. The beginning of the welding process (current flow) was of particular importance as regards the achievement of the assumed goals.

Figure 2, showing the numerical model (3D), presents mesh nodes (431, 415, 403) used in the analysis of the waveforms of characteristic quantities (temperature and current density).

The SORPAS software parameters adopted in the numerical calculations are presented in Table 2.

2.3 Process parameters

Based on the present recommendations and guidelines concerning the projection welding of nuts, the following range of welding parameters was adopted in relation to:

I) PFS [22–24]: (i) current $I = 16.0 \div 20.0$ kA, (ii) current flow time $t_{weld} = 10$ ms (up-slope) + 200 ÷ 300 ms (primary welding time) and (iii) electrode force $F = 5.0 \div 9.0$ kN,
II) EFS: (i) current $I = 14.0$ kA, (ii) current flow time $t_{weld} =$ 10 ms (up-slope) + 200 ÷ 300 ms and (iii) electrode displacement control during the flow of current.

For comparative purposes, also a current of 14.0 kA was subjected to analysis (in relation to the PFS). However, the above-named force was overly low and precluded the making of a proper welded joint.

In total, 15 variants, i.e. 12 in relation to the PFS (P1 ÷ P12) and 3 in relation to EFS (E1 ÷ E3) were subjected to analysis. The analysed variants along with preset welding parameters and the torsional moment obtained in destructive tests (M_B) are presented in Table 3.

The FEM calculations involved the adoption of material data from the (SORPAS) software database [18, 19]:

i) Nut: AISI 1017IW.Nr.1.0037 (Hr): $C_{0.20}Mn_{0.6}$: solidus, 1500 °C; liquidus, 1510 °C (Table 4)
ii) Sheet: HSLA 420-SAE J2340 420X-420LAD: solidus, 1500 °C; liquidus, 1510 °C (Table 5)
iii) Electrode: grade A3-1 (Table 6)

2.4 Experimental tests

The technological welding tests involved the making of a nut-sheet welded joint, frequently used when joining car body elements. Nut M10 × 22 × 10 (SAE 1015) with three symmetrically arranged projections (total base of projections amounted to 65 mm^2) was welded to 2.5 mm-thick sheet made of DKP-S550MC-O (PN-EN-10149-2) (without protective coating) [25], 300 mm × 3000 mm, at 50 mm intervals. Before welding, the sheet was degreased using a piece of flannel cloth. The chemical compositions of the welded materials (nut and sheet) are presented in Tables 7 and 8, respectively. The technological welding tests were performed using an inverter welding machine (1 kHz), the PFS (Fig. 3a) and EFS (Fig. 3b).

The results obtained in numerical calculations were verified experimentally in technological welding tests, metallographic tests, hardness measurements of the welding area (hardness map) and torsion tests as well as through measurements of selected characteristic parameters of the welding process including welding current and voltage, displacement of electrodes (projection height reduction) and electrode force. Characteristic parameters were recorded using a LogWeld-4 measuring device (Fig. 4). The functions of the measuring

Table 1 Dimensions of the nut

d	dc	h	h1	k	S	L	m
8.0 mm	21.75 mm	2.80 mm	1.10 mm	9.75 mm	15.00 mm	7.30 mm	3.00 mm

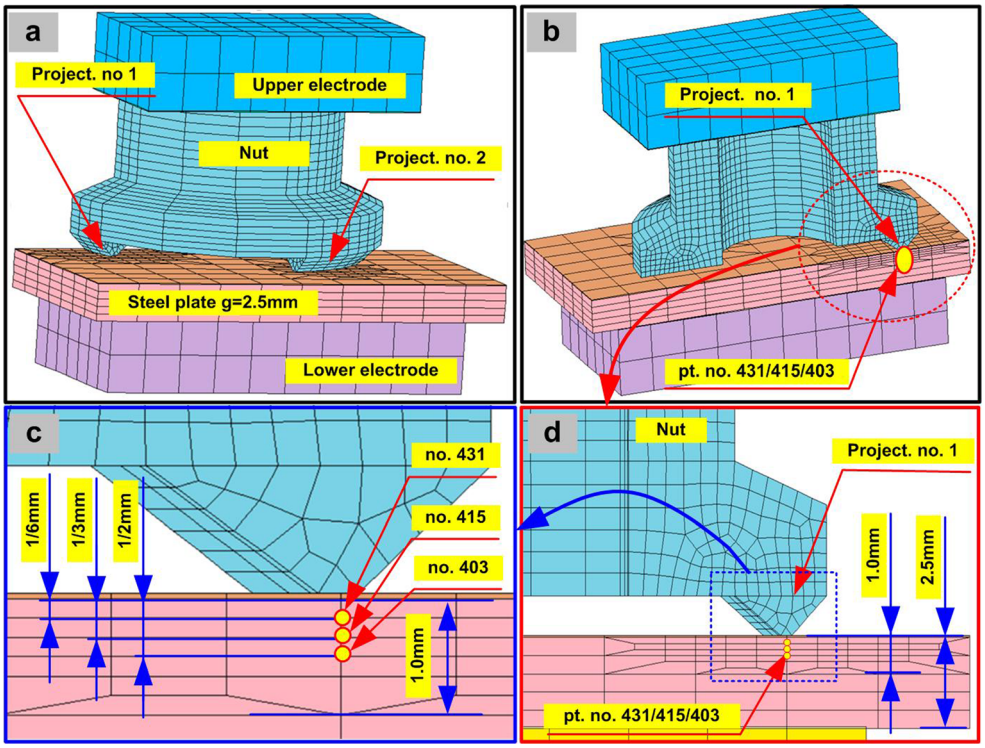

Fig. 2 Three-dimensional model with the FEM mesh and points (nodes) for analysis

device also enabled the performance of the analysis of (current and voltage) derivative parameters, e.g. waveform of static slope resistance, momentary power and energy supplied to the welding area. The above-named parameters referred to the entire welding area. The device also featured the analysis of waveforms, i.e. reading of momentary values and recorded variable values in relation to a time span marked using the cursor.

The specimens used in the metallographic tests were subjected to chemical etching using Nital. The parameters preset in relation to the PFS (grey) and two most favourable variants are presented in Table 9 (P7, P11). The remainder of Table 9

Table 2 Parameters used in the numerical calculations

	Initial squeeze	Current up-slope (increase)	Current flow time	Final squeeze	
Pneumatic force system (PFS)	500	10–70	200	500	ms
Electromechanical force system (EFS)	200	10	250–300	500	ms
Increment	1	0.2	0.2	1	ms
Data recorded at	2	2	1	2	Step
Convergence of calculations					
Accuracy of calculations					
Electrical model		1.00E−5			
Thermal model		1.00E−5			
Mechanical model		1.00E−5			
Heat emission (losses) to the environment					
Ambient (air) temperature		20		°C	
Heat transfer coefficient		300		W/m^2*K	
Other parameters					
Electrode dimensions (diameter)		30		mm	
Electrode height		10		mm	
Type of welding current		DC (1 kHz)			
Type of contact between welded elements		Sliding			

Table 3 Analysed variants in the numerical model and technological welding tests

No.	Variant	Electrode force system	Welding parameters			Remarks
			Current kA	Time ms	Force kN	
1	P1	Pneumatic (PFS)	14.0	200	5.0	$M_B < 50$ Nm
2	P2				7.0	
3	P3				9.0	
4	P4		16.0		5.0	$M_B < 200$ Nm
5	P5				7.0	$M_B < 150$ Nm
6	P6				9.0	$M_B < 50$ Nm
7	P7		18.0		5.0	OK, $M_B = 220$ Nm
8	P8				7.0	$M_B < 200$ Nm
9	P9				9.0	$M_B < 150$ Nm
10	P10		20.0		5.0	Thread deformation, expulsion
11	P11				7.0	OK, $M_B = 220$ Nm
12	P12				9.0	Thread deformation
13	E1	Electromechanical (EFS)	14.0	250	forging 6.0	OK, $M_B = 230$ Nm
14	E2			300	forging 6.0	OK, $M_B = 270$ Nm
15	E3			300	forging 9.0	OK, $M_B = 300$ Nm

presents characteristic parameters describing the welding process. These parameters included energy supplied to the welding area, a breaking torque (M_B) as well as the width and depth of the weld. Unfavourable effects such as expulsion, nut thread deformation or the overheating on the other side of the sheet were not observed in relation to the above-named parameters. In both cases the mean value of the breaking torque in the torsion test amounted to 220 Nm.

2.5 Process optimisation

The optimisation of the projection welding of nuts was performed experimentally in technological welding tests using the EFS. The primary optimisation-related approach included the reduction of welding current and the extension (where/if necessary) of welding current flow. The optimisation concerning the EFS involved the adjustment of lower electrode force at the beginning of the welding process and controlling the displacement of electrodes during the current flow. The above-named adjustment and control aimed to obtain the most favourable space distribution of welding power enabling the emission of appropriately more heat (energy) in the contact area between the elements being joined, i.e. the projection and the nut, and, consequently, the more intense melting of the materials being welded.

The preset parameters in relation to the EFS (grey) are presented in Table 10. The technological welding tests were performed using significantly lower current (14.0 kA) than that applied when welding was performed using the PFS. As regards the PFS, the above-named welding current value, within the entire range of analysed electrode force of 5.0 to 9.0 kN, resulted in the obtainment of unacceptable values of a breaking torque of less than 50 Nm.

Table 10 presents three exemplary analysed variants (E1 ÷ E3). The technological welding tests were performed using a current of 14.0 kA. Parameters modified during the process included the time of current flow, the displacement of electrodes and the value of upsetting (forging) force. Because of significantly many preset parameters and in order to demonstrate differences between individual variants in a more favourable manner (i.e. changed values of parameters), values not changed in the subsequent variant (line in Table 10) were presented using the sign of "–". Such presentation of data enabled the author to analyse data relatively quickly.

3 Results

Presented below are the results of the numerical calculations and experimental tests concerning the analysed process of the projection welding of nuts (to sheets) in relation to two analysed electrode force systems, i.e. PFS and EFS.

3.1 FEM calculation results

Analyses were performed in relation to 12 variants connected with the PFS (P1 ÷ P12) and three variants related to the EFS (E1 ÷ E3). Table 11 presents numerical results concerning the two electrode force systems. The welding process performed using the PFS was analysed with reference to the electrode

Table 4 Material properties of nut (AISI 10017/W.Nr.1.0037) (Hr): $C_{0.20}Mn_{0.6}$)

Temperature (°C)	Thermal conductivity (W/m*K)	Temperature (°C)	Heat capacity (J/kg*K)	Temperature (°C)	Resistivity (μΩ*m)	Temperature (°C)	Mass density (kg/m^3)	Temperature (°C)	Thermal expansion coefficient (10^{-6}/°C)	Temperature (°C)	Young's modulus of elasticity (kN/mm^2)
0	51.9	100	481	20	0.159	20	7870	100	12.2	25	200
100	50.8	400	597	100	0.219			400	13.5		
200	48.9			200	0.293			600	14.5		

Table 5 Material properties of sheet (HSLA 420-SAE J2340 420X-H420LAD)

Temperature (°C)	Thermal conductivity (W/m*K)	Temperature (°C)	Heat capacity (J/kg*K)	Temperature (°C)	Resistivity (μΩ*m)	Temperature (°C)	Mass density (kg/m^3)	Temperature (°C)	Thermal expansion coefficient (10^{-6}/°C)	Temperature (°C)	Young's modulus of elasticity (kN/mm^2)
20	51.9	50	472	20	0.159	20	8020	100	11.9	25	200
100	51.7	150	506	100	0.205			200	12.7		
200	50.0	200	522	200	0.277			400	13.9		
300	48.0	250	538	400	0.465			600	14.7		
400	45.2	300	559	600	0.745			800	12.1		
500	42.2	350	584	800	1.083			1000	13.8		
600	38.8	450	642	1000	1.158						
700	33.8	550	773	1200	1.212						
800	30.0	650	828	1400	1.234						
1000	30.7	700	1439								
		750	812								
		850	530								

Table 6 Material properties of electrode (ISO 5182 A3/1 electrode CuCoBe)

Temperature (°C)	Thermal conductivity (W/m*K)	Temperature (°C)	Heat capacity (J/kg*K)	Temperature (°C)	Resistivity (μΩ*m)	Temperature (°C)	Mass density (kg/m^3)	Temperature (°C)	Thermal expansion coefficient (10^{-6}/°C)	Temperature (°C)	Young's modulus of elasticity (kN/mm^2)
20	225	20	420	20	0.055	20	8750	25	16.5	25	117
100	217	127	446	100	0.060	1080	8000				
200	210	327	466	200	0.071						
300	203	527	482	300	0.075						
400	196	727	500	400	0.082						
500	190	927	529	500	0.090						
600	183			600	0.098						
700	177			700	0.106						
800	171			800	0.115						
900	165			900	0.124						
1000	160			1000	0.135						
1100	154			1100	0.254						
1200	149			1200	0.260						
1300	143			1300	0.266						

Table 7 Chemical composition of nut M10x22x10 (SAE 1015, wt.%)

C	Mn	P	S	Fe
0.17	0.44	0.013	0.008	Bal.

force range of 5.0 to 9.0 kN (every 2.0 kN), the welding current range of 14.0 to 20.0 kA (every 2.0 kA) and a welding time of 200 ms.

The analysis was performed in relation to the maximum current flow time amounting to 200 ms. This was because of the fact that the extension of time did not result in an increase in the most important joint-related parameters, i.e. the width and height of the joint. In turn, as regards the EFS, the analysis was performed in relation to the same value of current (14.0 kA) but for various welding times restricted within the range of 250 to 300 ms and various electrode displacement trajectories. In addition, the end of the welding process was accompanied by the introduction of an upsetting force of 6.0 and 9.0 kN. The parameters subjected to analysis included (i) weld width, (ii) weld height (penetration depth in the sheet), (iii) volume of molten material weld nugget) and (iv) displacement of electrodes during the flow of current and at the end of the process.

Figure 5 contains the graphic representation of the FEM calculation results presented in Table 11 and the technological welding test results in relation to the PFS.

Figure 6 presents calculation results, i.e. temperature distribution, concerning the two selected variants, i.e. P7 (related to the PFS) and E1 (related to the EFS).

The distribution of temperature was presented in one of the SORPAS software modes, i.e. in the so-called *pick temperature* mode. This result presentation mode presents ("remembers") the maximum temperature occurring in a given area within a given welding cycle.

Figure 7 presents selected comparative results concerning numerical calculations related to the PFS and EFS, i.e. electrode force and displacement, momentary power, static slope resistance, the course of temperature, the volume of the molten metal and the weld nugget area.

Figure 8a presents comparative courses of temperature in relation to the PFS and EFS. The courses are presented for the selected numerical model mesh nodes (Fig. 2c) located centrally in the sheet, under the projection, being 1/6 mm (node 431), 1/3 mm (node 415) and 1/2 mm (node 403) away from the upper surface of the sheet respectively. In turn, Fig. 8b presents the waveforms of the dynamic resistance and momentary power in relation to the entire welding area.

Table 8 Chemical composition of sheet DKP-S550MC-O (1434, wt%)

C	Mn	P	S	Si	Al.	Nb	V	Ti	Fe
0.065	0.91	0.008	0.007	0.014	0.032	0.063	0.003	0.039	Bal.

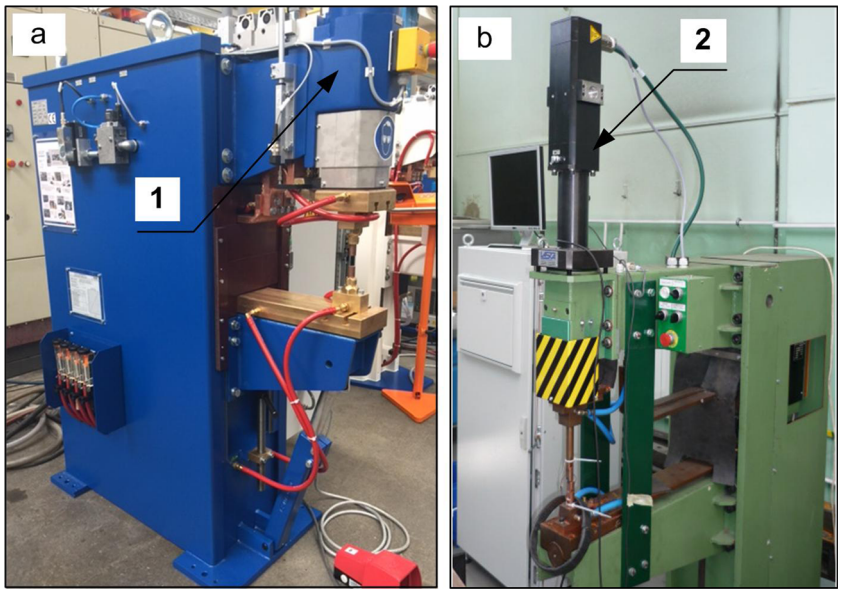

Fig. 3 Test rig for technological welding tests provided with: **a** PFS and **b** EFS: (1) pneumatic actuator and (2) servomotor

3.2 Experimental test results

The technological welding tests were performed for all (15) of the variants subjected to analysis (Table 3). Selected results in the form of metallographic structures of the welded joints are presented in:

- Figure 9, in relation to the PFS-variant P7,
- Figure 10, in relation to the EFS-variant E1.

4 Discussion

Before the principal discussion, it is necessary to characterise the correlation between the electrode force and the electrode displacement, i.e. the basis of the optimisation related to the analysed resistance projection welding of nuts.

In cases of projection welding performed using the classical PFS, the preset parameter is the constant value of actuator pressure, which, theoretically, translates into the constant value of preset force and results in the displacement of electrodes tantamount to projection height reduction. Parameters adjusted before the process of welding, i.e. current, current flow time and electrode force, are decisive for the final outcome related to the movement, i.e. displacement of electrodes. It should be noted that because of the high inertia of the PFS it is not possible to control electrode force or displacement during welding.

An alternative solution enabling the improvement of the welding process involves the use of the EFS and the application of an appropriate (hybrid) algorithm enabling the control of electrode force and/or displacement and characterised by (i) adjustment of electrode force before the flow of current; force being lower than that applied using the PFS, (ii) control of electrode displacement during the welding current flow and (iii) exertion of upsetting force after current decay. The most important factors characterising the EFS include the possibility of slowing down the movement of electrodes and the follow-up control of electrode displacement (particularly during the flow of current) [26, 27].

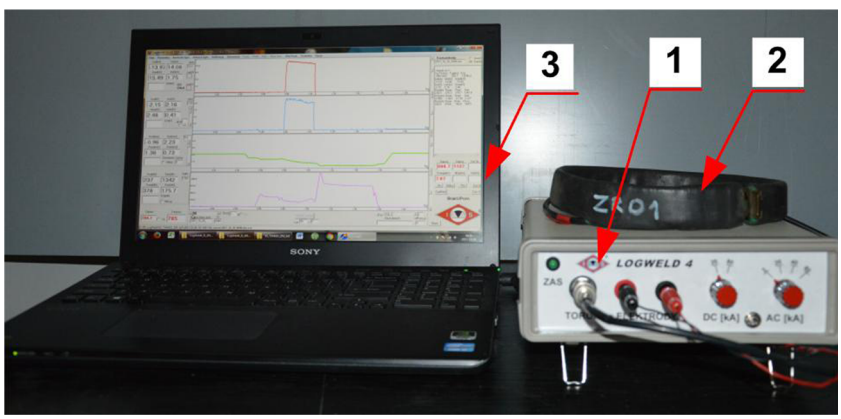

Fig. 4 LogWeld-4 device for measurements of characteristic parameters of the resistance welding process, (1) measurement interface, (2) Rogowski coil and (3) PC

Table 9 Preset parameters and characteristic parameters in relation to the PFS

No.	Variant No.	Preset parameters							Recorded parameters					
		Force	Up-slope		Main welding time		Total current (I_{rms})	Main interval current (I_{rms})	Energy	Projection height reduction	Weld width	Weld height	Breaking torsional moment (M_B)	Number of specimens
			Current	Time	Current	Time								
		kN	kA	ms	kA	ms	kA	kA	kJ	mm	mm	mm	Nm	pcs
		A	B1	B2	C1	C2	D1	D2	E	F	G	H	I	J
1	P7	5.0	18.0	50	18.0	150	17.8	13.0	8.3	0.74	2.1	0.05	220	30
2	P11	7.0	20.0	50	20.0	150	19.7	20.0	9.5	0.95	2.1	0.06	220	3C

I_{rms}, root-mean-square current

The application of the hybrid algorithm (instead of the classical PFS) enabled the obtainment of favourable conditions as early as at the very beginning of the flow of welding current. Lower electrode force resulted in (i) lower cold projection height reduction (before current flow), (ii) increase in contact resistance, (iii) higher power and (iv) generation of higher energy in the most favourable area, i.e. in the contact area between elements being welded. Subsequently, during the flow of current, the control of electrode displacement and the slowing down of electrode movement resulted in the obtainment a less contact area between elements being welded and, consequently, higher resistance in the contract area. The foregoing enabled the more intense heating and, consequently, the melting of the materials subjected to welding, whereas the use of the PFS only enabled the obtainment of material plasticisation.

The slowing down of electrode movement translated into a favourable decrease in the rate of projection height reduction. The time of welding could be extended, which significantly affected the generation of welding power in the most important areas, i.e. in the projection material and in the contact area between materials being welded. In spite of the lower value of welding current, the extension of projection height reduction time led to the generation of higher welding power in the projection material [16].

4.1 FEM calculations

The PFS-related results detailed in Table 11 are presented graphically in Fig. 5. Only two variants, the P7 and P11 met the acceptance criterion, i.e. the obtainment of a breaking torque (M_B) of 220 Nm. The above-presented torque value was determined experimentally in related strength tests performed using the welded test specimens (Fig. 5h). The results shown in Fig. 5a–g present the variability of characteristic parameters obtained in the numerical model. Figure 5a–g presents (i) weld width, (ii) displacement of electrodes at the end of the flow of current, (iii) weld height, (iv) displacement of electrodes at the end of the welding process, (v) penetration depth, (vi) energy supplied to the welding area and vii) weld nugget volume respectively.

The analysis of the PFS-related results (Fig. 5) indicates a narrow window of parameters. The comparative analysis was performed using variant P7, requiring less welding current. The above-named variant was subjected to the comparative analysis with selected variant E1 related to the EFS. Figures 6 and 7 present the comparative analysis in relation to selected variants P7 and E1. Figures 6 and 7 present the distribution of temperature during the welding process and courses/waveforms of characteristic parameters (electrode force and displacement, momentary power, dynamic resistance, temperature, the volume of the weld nugget molten material and the surface of weld nugget, respectively).

The images presenting the distribution of temperature during the flow of current in the welding process performed using the PFS (Fig. 6 (a1–a6)) revealed the very slight melting of the material. At the beginning of the welding time (up to 50 ms) the melting of the material was not observed (Fig. 6 (a1/a2)). The foregoing could be attributed to the excessive cold projection height reduction (i.e. before the flow of current) and fast projection material plasticisation. The above-named factors increased the unfavourably large contact area between the welded elements (projection and sheet), which decreased the density of current to a level precluding the melting of the material. Figure 6 (a7) present the total molten material area in relation to variant P7, where the weld nugget height amounted to a mere 0.15 mm, whereas the width amounted to approximately 1.1 mm.

For comparison, Fig. 6 (b1–b6) presents the distribution of temperature during the flow of current in the welding process performed using the EFS. Within the entire range of welding current flow, particularly at the very beginning, it was possible to observe the melting of the material. The foregoing indicates that, in spite of a lower welding current of 14.0 kA, the process provided better conditions for the melting of the material. The use of the EFS and the application of the hybrid algorithm resulted in the obtainment of the greater total area and volume of molten material, where the weld nugget height amounted to

Table 10 Preset parameters and characteristic parameters in relation to the EFS

Variant No.	Preset parameters															Recorded parameters						
	Force			Up-slope		Main welding time			Total current (I_{ms})	Main interval (I_{ms})	Time and displacement of electrodes					Upsetting force (forging)	Energy	Projection height reduction	Weld width	Weld height	Breaking torsional moment (M_B)	Number of specimens
	Initial	Minimum	Maximum	Current	Time	Current	Time				$t_1/\Delta l_1$	$t_2/\Delta l_2$	$t_3/\Delta l_3$	$t_4/\Delta l_4$								
	kN			kA	ms	kA	ms		kA	kA	ms/mm					kN	kJ	mm	mm	mm	mm	pcs
	A1	A2	A3	B1	B2	C1	C2	D1	D2	E1	E2	E3	E4	F	G	H	I	J	K	L		
1	E1	3.5	2.5	6.3	14.0	10	14.0	240	14.1	14.4	15 0.05	110 0.03	75 0.15	50 0.3	6.0	6.7	0.71	2.9	0.50	230	30	
2	E2	–	–	–	–	–	–	290	–	–	–	–	–	100 0.3	6.0	7.5	0.75	3.0	0.53	270	30	
3	E3	–	–	–	–	–	–	–	–	–	–	–	–	–	9.0	7.5	0.9	3.1	0.55	300	30	

I_{rms}, root-mean-square current, "–" value identical as in the line above

approximately 0.42 mm, whereas its width amounted to 2.3 mm (Fig. 6 (b7)).

The obtainment of more favourable conditions resulted from the use of the EFS and the hybrid algorithm enabling the control of electrode displacement. The melting of the material proved more intense despite the fact that lower welding current was used. Figure 7 presents waveforms/courses of the welding process characteristic parameters. Figure 7 (a1/b1) presents the waveforms/course of (i) welding current, (ii) electrode displacement and (iii) electrode force. The use of the EFS involved the control of electrode displacement (curve 2b). Importantly, the projection height reduction obtained when using the EFS (ΔL_{EPHRC}) only amounted to 0.04 mm (Fig. 7 (b1)), whereas, as regards the PFS (ΔL_{PPHRC}), it amounted to 0.23 mm (Fig. 7 (a1)). The use of the above-presented "trick" at the very beginning of the flow of current created significantly more favourable welding conditions. The control of electrode displacement led to the obtainment of an appropriate course of electrode force (Fig. 7 (b1, curve 3b)). Force values obtained when using the EFS were lower than those obtained using the PFS (Fig. 7 (a1, curve 3a)). The lower EFS-related force values translated into the smaller contact area between the elements being welded. The greater resistance of the entire welding area combined with the lower value of electrode force resulted in an increase in resistance, primarily in the contact area between the elements being welded. The foregoing resulted in higher resistance (Fig. 7 (b2, curve 4b)), particularly visible at the beginning of the time of current flow ($R_E = 420\ \mu\Omega$), than the resistance obtained using the PFS (Fig. 7 (a2, curve 4a), $R_P = 300\ \mu\Omega$). Next, it was possible to observe the generation of higher welding power, particularly important at the beginning of welding (the first 50 ms, Fig. 7 (a2/b2, curves 5a/5b)), providing conditions for the more intense melting of the material (Fig. 6 (b1)). The effectiveness of the EFS control was confirmed by the greater ultimate area of the weld (Fig. 7 (b3, curve 6b)) and the greater volume of the molten material, i.e. the weld nugget (curve 7b), in comparison with those obtained using the PFS (Fig. 7 (a3, curves 6a and 7a, respectively)). The weld area obtained using the EFS was by twice larger than that obtained using the PFS ($S_E = 53.2\ mm^2$, $S_P = 24.0\ mm^2$). In turn, the volume of the weld nugget material was four times greater ($V_E = 21.0\ mm^3$, $V_P = 4.7\ mm^3$). The higher efficiency of the heating (or, more precisely, melting) of the material was demonstrated by the course of temperature in relation to (mesh) node No. 403 of the numerical mesh model (Fig. 2). The above-named node was located below the projection, in the sheet, 0.5 mm away from the upper surface of the sheet. In relation to the EFS (curve 8b), it was possible to observe the exceeding of the sheet melting point

Table 11 Preset parameters and characteristic result of FEM calculations for PFS and EFS

			Pneumatic system (PFS)												Servo system (EFS)		
Preset parameters																	
1	(a) Force	kN	5				7				9				–		
	(b) Displacement	mm	–				–				–				0,65	0,7	0,7
2	Welding time	ms	200				200				200				250	300	300
3	Welding current	kA	14	16	18	20	14	16	18	20	14	16	18	20	14		
4	Variant number		P1	P4	P7	P10	P2	P5	P8	P11	P3	P6	P9	P12	E1	E2	E3
Characteristic quantities																	
5	Nugget width	mm	0.81	1.58	2.31	2.92	0.42	0.62	0.96	1.88	0.35	0.54	0.92	1.31	2.8	2.8	2.9
6	Depth of penetration in the sheet	mm	0.04	0.07	0.07	0.07	0.02	0.04	0.05	0.06	0.01	0.03	0.05	0.05	0.45	0.5	0.5
7	Height of the nugget	mm	0.05	0.07	0.07	0.11	0.02	0.05	0.05	0.07	0.01	0.03	0.05	0.07	0.50	0.55	0.55
8	Electrode displacement at the end of current flow	mm	0.45	0.56	0.66	0.76	0.61	0.65	0.80	0.92	0.71	0.79	0.96	1.11	0.25	0.25	0.25
9	Displacement of electrodes (final)	mm	0.51	0.67	0.82	1.00	0.54	0.78	1.00	1.12	0.62	0.94	1.12	1.13	0.70	0.75	0.85
10	Nugget volume	mm^3	0.83	2.34	3.58	6.23	0.14	0.40	1.05	2.81	0.03	0.39	1.01	1.67	16.2	18.1	18.1
11	Energy	kJ	6.37	7.64	8.90	10.24	6.04	7.26	8.50	9.84	5.80	7.01	8.40	9.58	7.0	7.5	7.5

(solidus 1500 °C) and the obtainment of the maximum temperature of 1560 °C. The maximum temperature obtained using the PFS amounted to 1284 °C (curve 8a). The analysis of related temperature courses demonstrated deeper penetration, i.e. the greater height of the weld nugget.

4.2 Experimental tests

4.2.1 Waveforms/courses of characteristic parameters

The results of the experimental tests, in the form of recorded characteristic parameters (current, electrode force and displacement, momentary power and dynamic resistance), concerning the two analysed electrode force systems are presented in Fig. 11.

The above-presented variant P7 is concerned with the PFS, whereas variant E1 is concerned with the EFS. A significant difference, resulting from the adopted approach to optimisation, was the lower value of welding current (obtained when the EFS was used) amounting to 14.0 kA.

Figure 11 presents the results concerning the PFS (on the left) and those related to the EFS (on the right). It is possible to notice differences in welding current waveforms in relation to the analysed electrode force systems. The technological welding tests involving the use of the PFS were performed using a DALEX welding machine (Fig. 3a) with the maximum adjusted current up-slope rate. An effect in the form of delayed current up-slope presented in Fig. 11 (a1, curve 3a1) resulted from restrictions connected with the current up-slope rate, which in turn, was related to the reactance of the secondary circuit and software-hardware protections of the welding machine. In order to control welding current during welding performed using the PFS it was necessary to adopt a similar welding current envelope (Figs. 7 (a1–a4) and 8a, b). The rate of the initial current up-slope was higher in relation to the welding machine provided with the EFS (Figs. 3b and 11 (b1, curve 3b1)).

In relation to the PFS, the value of force was constant, amounted to 5.0 kN (Fig. 11 (a1, curve 2a1)) and led to the obtainment of the resultant displacement of electrodes (Fig. 11 (a1, curve 1a1)). In terms of the total displacement of electrodes, it is necessary to take into account the value of cold projection height reduction. The above-named value, amounting to approximately 0.3 mm, is not visible in Fig. 11 (a1). In turn, in relation to the EFS (Fig. 11 (b1/b2)), the displacement of electrodes was subjected to control (curve 1b1) and force was a resultant element (curve 2b1). Nearly within the entire range of a current flow time of 240 ms, the course of force (Fig. 11 (b1, curve 2b1)) amounted to less than 5.0 kN, i.e. was below the value of force obtained using the PFS (Fig. 11 (a1, curve 2a1)). Figure 11 (a2 and 11b2) present the waveforms of resistance (curve 1a2/1b2) and momentary power (curve 2a2/2b2) in relation to both cases (PFS and EFS). The waveforms of resistance and momentary power refer to the entire welding area. The resistance is greater (especially at the beginning of current flow), whereas the waveform and the maximum momentary power were significantly lower (Fig. 11 (a2/b2, curve 2a2/2b2), in relation to the EFS. As regards the EFS, lower power resulted from the lower value of current. However, the melting of the greater weld nugget area (Fig. 10) combined with the lower value of power constituted a significant advantage of the applied solution (algorithm enabling the control of displacement) but also came as a surprise.

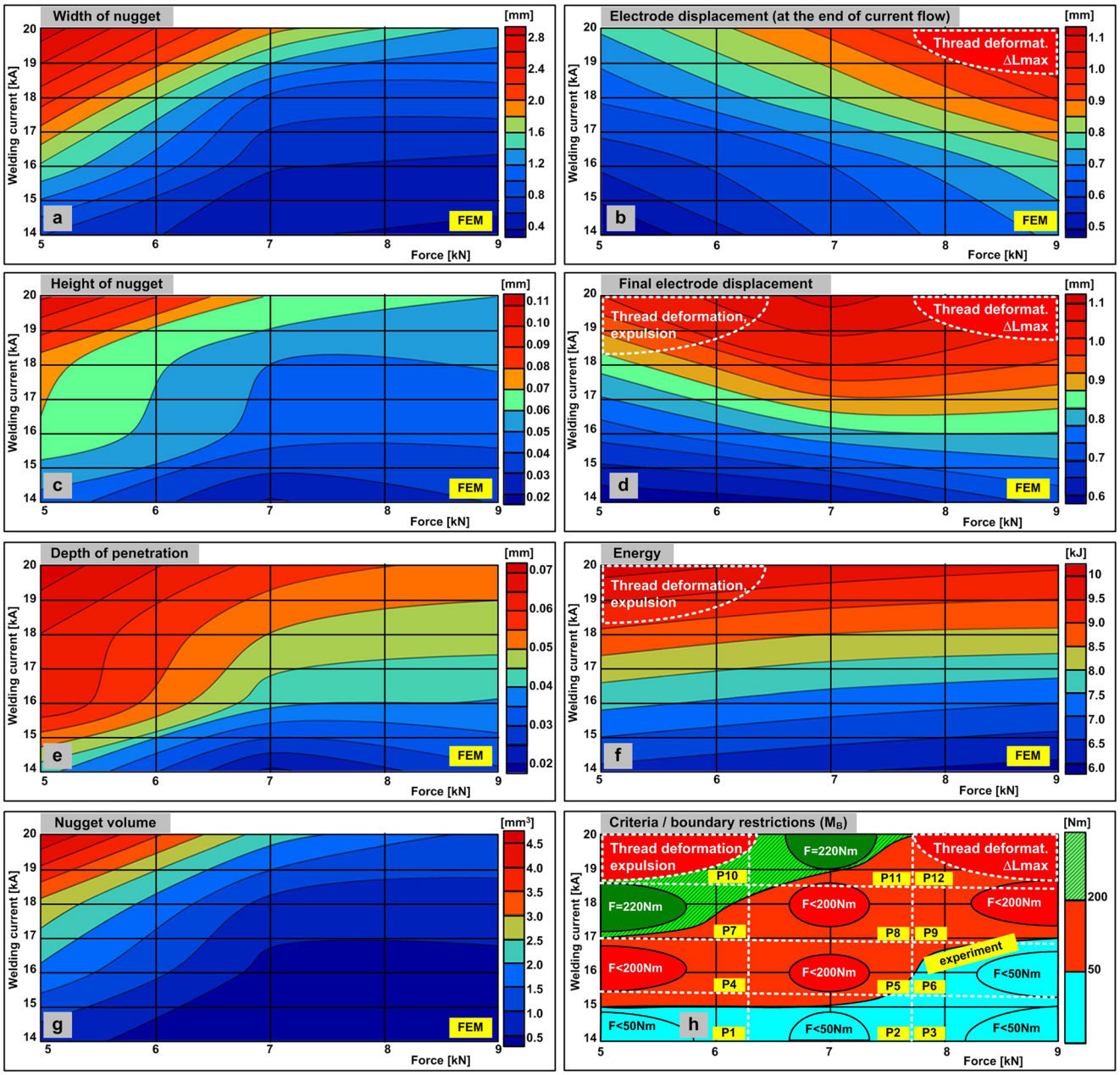

Fig. 5 Graphic representation of numerical calculation results listed in Table 11 in relation to the PFS and related boundary criteria

Figure 12 presents the EFS-related courses/waveforms of characteristic parameters recorded during the technological welding tests involving various EFS variants (Table 10, variants E1 ÷ E3).

The breaking torque related to the first analysed EFS variant amounted to 230 Nm (E1, Table 10 line 1, column K) and was slightly higher than the value obtained using the PFS (220 Nm) (P7, Table 9, line 1, column I). Already, the first analysed EFS (E1) satisfied the initial criterion related to torsional strength, where the breaking torque should be not less than that obtained in relation to the most favourable PFS-related (P7). The further EFS-related optimisation involved the extension of welding time from 250 to 300 ms (E2), which increased the breaking torque by approximately 17% (from 230 to 270 Nm). Variant E3 involved an increase in upsetting (forging) force from 6.0 to 9.0 kN, which, in turn, increased the torque by approximately 30% (from 230 to 300 Nm) in relation to variant E1. The energy supplied to the weld and the courses of electrode force related to variants E1 ÷ E3 are presented in Fig. 12 (a2, curves 1a2, 4a2, and 7a2) and in Fig. 12 (a3, curves 1a3, 3a3, and 5a3), respectively. The greatest displacement of electrodes (projection height reduction) was recorded in relation to variant E3 and a forging force of 9.0 kN (Fig. 12 (a1, curve 7a1)).

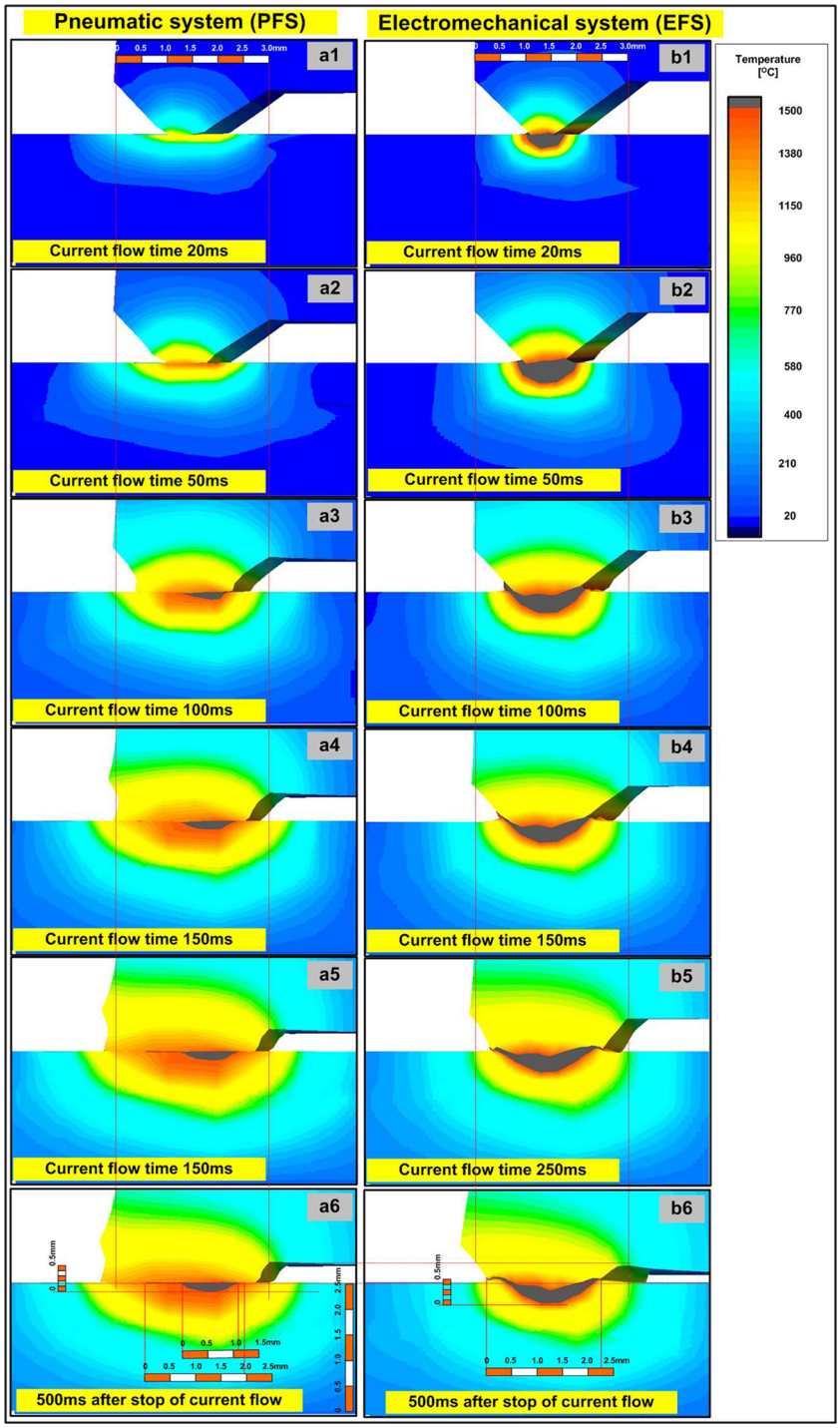

Fig. 6 Temperature distribution at selected moments of the welding process performed using the PFS (variant P7) and EFS (variant E1) (FEM)

The further process optimisation, involving the extension of welding time, resulted in expulsion and the overheating of the nut material on the side of contact with the upper electrode. Both phenomena led to the partial melting of the upper part of the nut and to the deformation of the thread.

The results presented in Table 10 revealed that, as regards the EFS and the applied hybrid algorithm, the decrease in welding current enabled the use of a welding machine having lower power and the obtainment of torsional strength not lower than that obtained using the PFS.

4.2.2 Metallographic tests and hardness measurements

The welding process-related characteristic courses/waveforms presented in Fig. 11 were recorded for the technological welding tests, in relation to which metallographic and

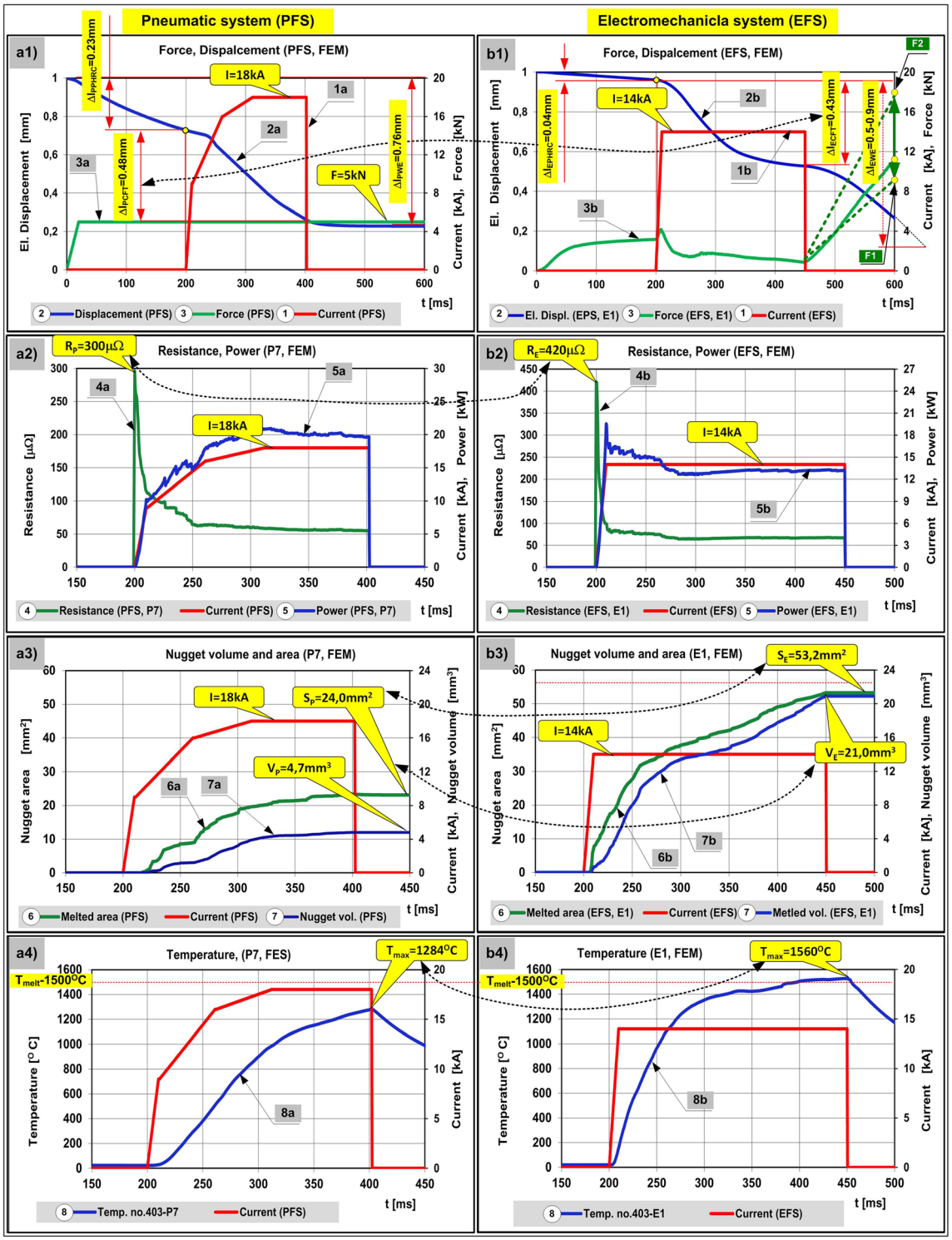

Fig. 7 Waveforms/courses of characteristic parameters in relation to: **a** PFS and **b** EFS (FEM)

hardness tests were performed. The hardness measurements were performed making a hardness map of the entire welding area, containing a total of 588 measurement points (21 lines, each having 28 points) (Fig. 13).

The metallographic test results (Figs. 9 and 10) confirmed the results previously obtained in the numerical calculations (Figs. 7 and 8) and indicating the possibility of obtaining more favourable temperature distribution and a greater sheet material melting area (volume) when slowing down the movement (displacement) of the electrodes.

Figure 14 presents the PFS (Fig. 14 (a1, P7)) and EFS-related metallographic structures (Fig. 14 (b1, E1)) along with

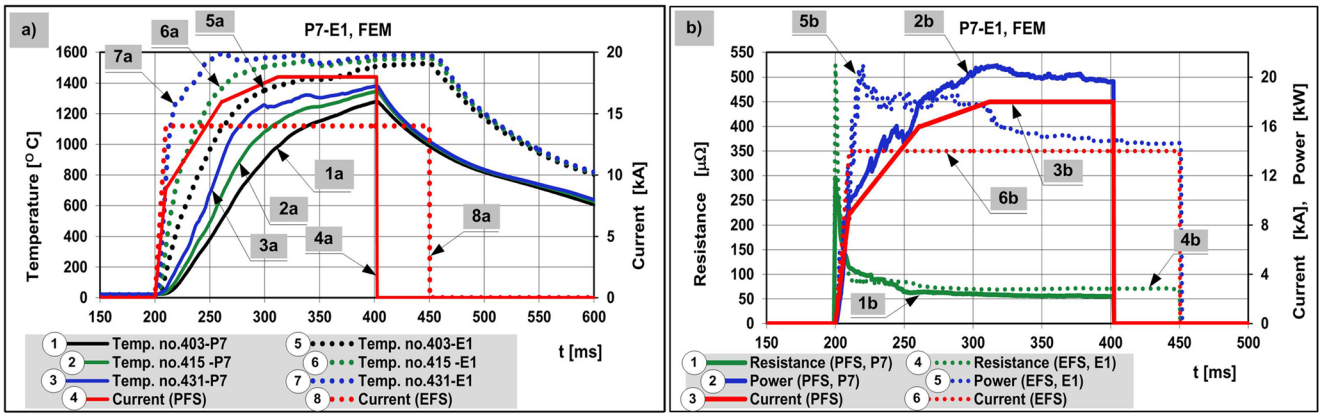

Fig. 8 Waveforms/courses of characteristic parameters in relation to the PFS and EFS: **a** temperature and **b** dynamic resistance, momentary power (FEM)

the hardness map (Fig. 14 (a2/b2)). The metallographic structure-related results presented in Figs. 9, 10 and 14 confirmed the melting of a greater area of the welded materials (greater width and height of the weld) when the EFS was used.

As regards the PFS, the height of the molten area of the weld (nugget) amounted to a mere 58 μm, whereas the width was 830 μm. The remainder of 2031 μm (recognised as a joint without the clearly visible stirring of the materials) constituted a solid-state joint (Fig. 9 (P2)).

As regards the EFS, the height of the molten area of the weld (nugget) amounted to 567 μm (ten times higher), whereas the width was 2976 μm. The material was molten across the entire width of the weld (Fig. 14 (b1)).

The tests concerning the distribution of hardness (Fig. 14 (a2/b2)) in relation to the PFS (P7) and EFS (E1) are the following:

1. As regards the PFS Fig. 14 (a1/a2 (P7)), a metallic joint was present only along length $A = 830$ μm. Outside the above-named area, the joint contained a zone without the clearly visible stirring of materials (typical of solid-sate joints). The above-presented phenomenon was not observed as regards the weld made using the EFS (Fig. 14 (b1/b2), where the width of the zone characterised by (clearly visible) stirring of materials amounted to $A = 2976$ μm.

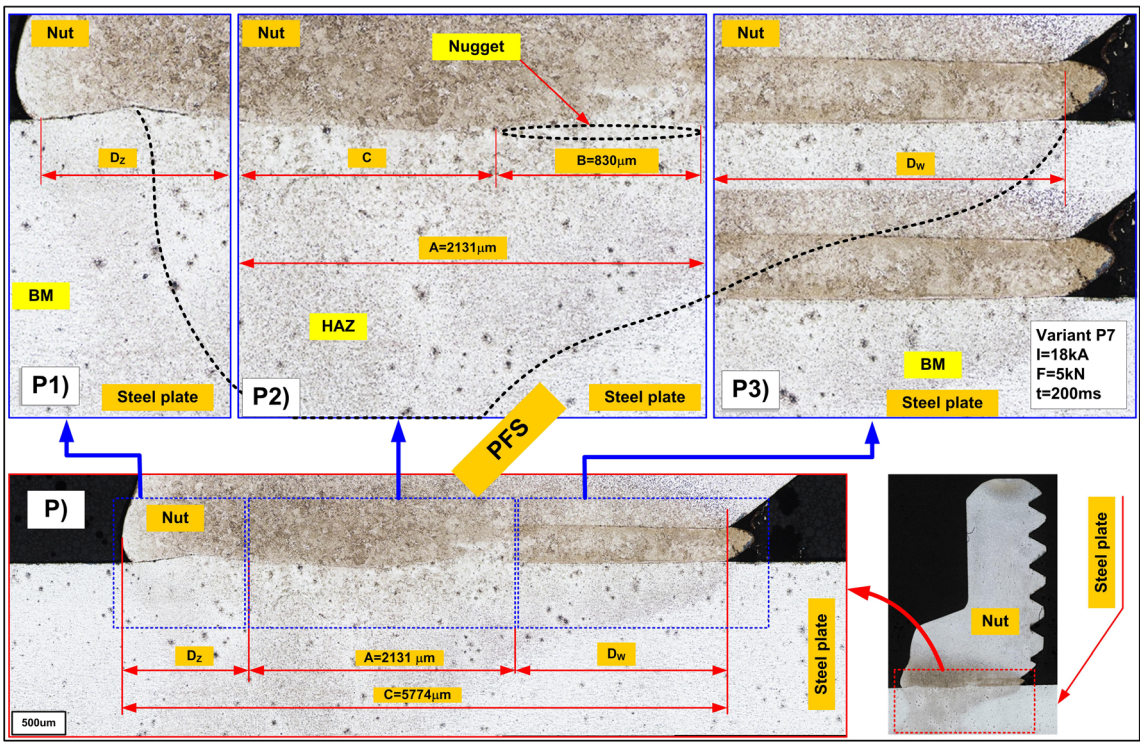

Fig. 9 Metallographic structure of the welded joint in relation to the PFS (variant 7)

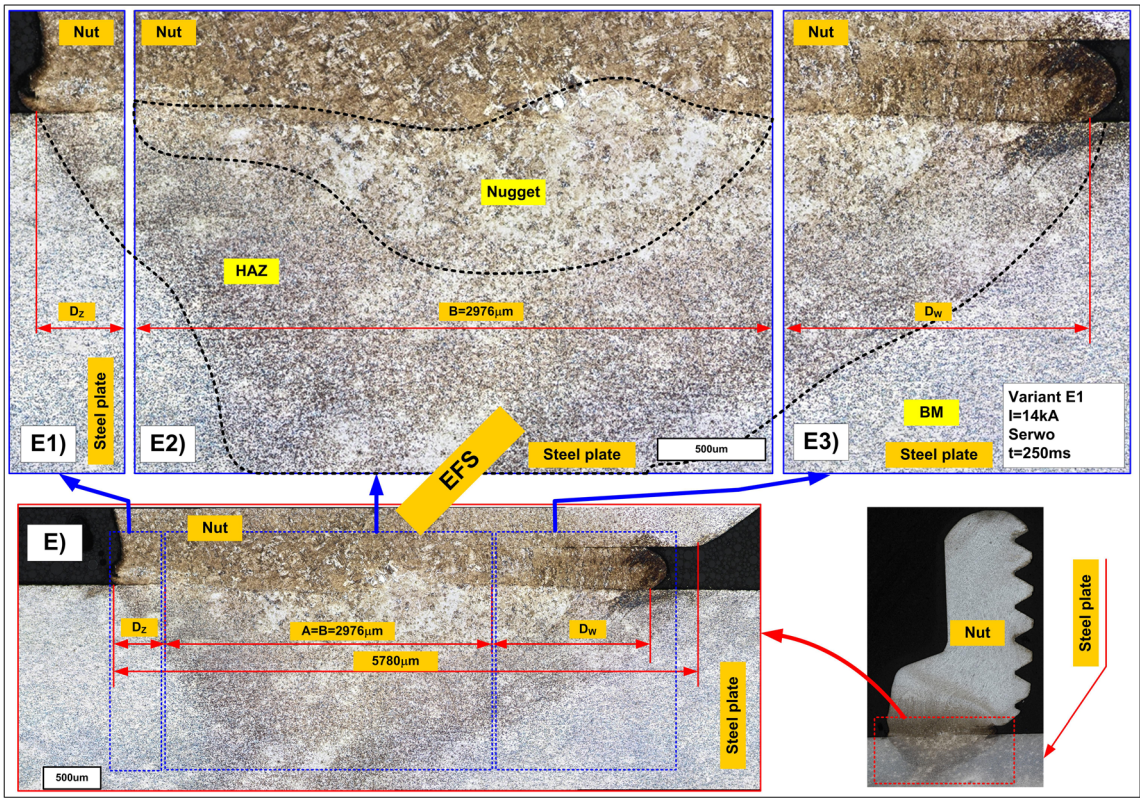

Fig. 10 Metallographic structure of the welded joint in relation to the EFS (variant E1)

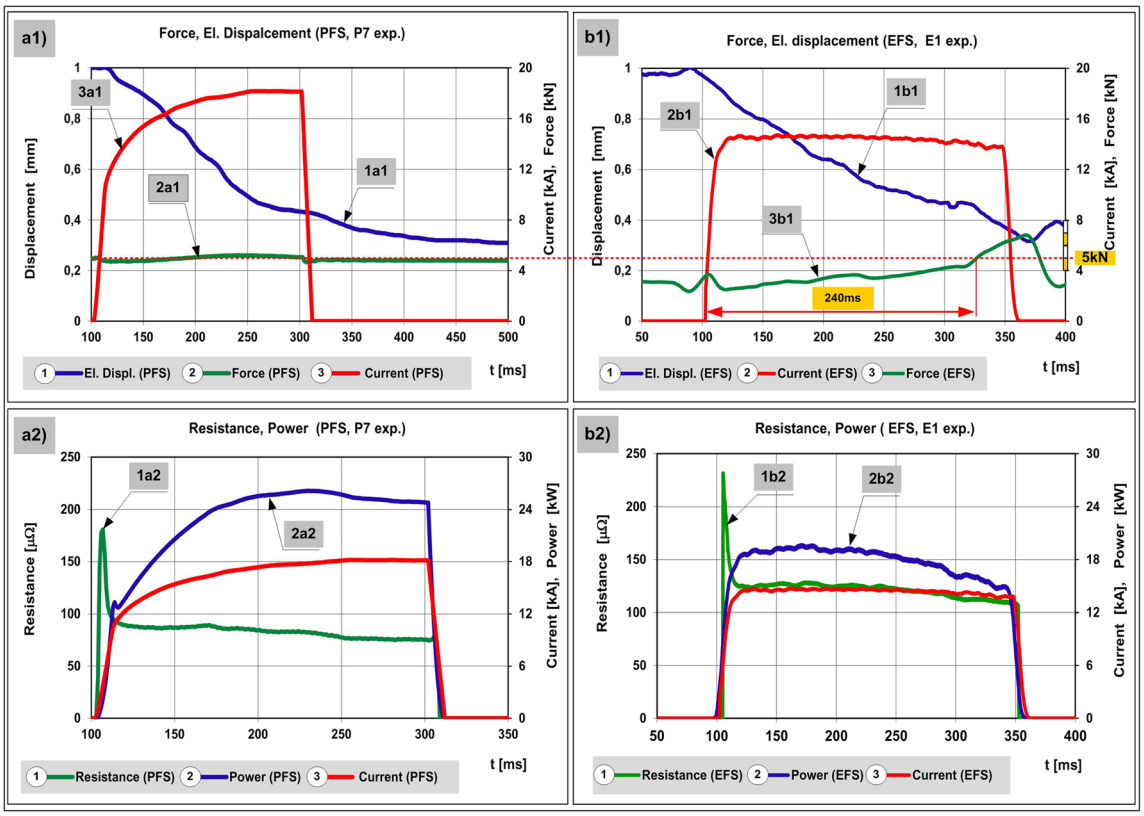

Fig. 11 Experimental waveforms/courses in relation to the two analysed electrode force systems: **a** PFS (P7) and **b** EFS (E1)

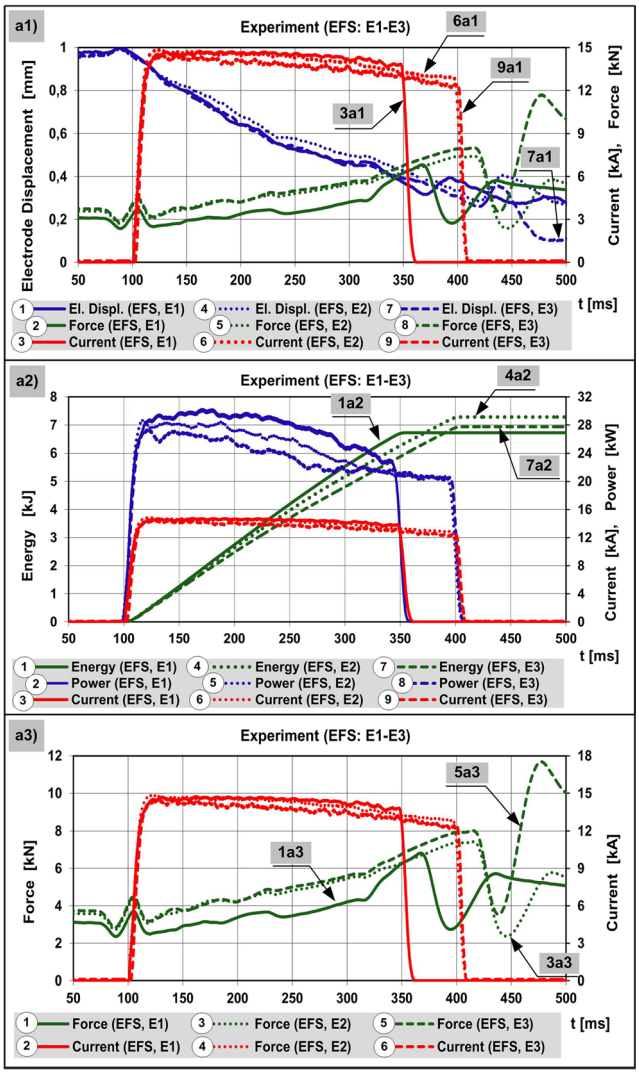

Fig. 12 Courses/waveforms of the characteristic parameters recorded during the technological welding tests in relation to variants E1 ÷ E3 (experiment)

2. Material continuity was observed in cases of the welds made using the EFS-Fig. 14 (b2 (E1)).
3. Variant E1 (EFS) was related to the lower hardness of the weld, which indicated higher plasticity in the welding area, translating into the lower tendency of joint cracking in operating conditions.
4. The area of the welded joint made using the EFS was deliberately provided with a higher heat input to melt greater material volume. However, the aforesaid action increased the HAZ, which could be perceived as a certain inconvenience when making projection welded joints as it could worsen mechanical properties of the sheet material.

4.3 Comparison of results

It was decided that the most favourable form of result presentation, making it possible to explain the essence of the phenomena occurring in the resistance welding process performed using the new electrode force system, would be the comparison of the experimental test results having the form of welded joint metallographic structures and of the numerical calculations having the form of courses of temperature at selected points of the welding area (Fig. 15) as well as the distribution of temperature in the welding area (Fig. 16).

The above-named comparison of the results was extended by the comparison of the characteristic parameters (current, momentary power, energy) recorded during the technological welding tests (Fig. 17) and the numerical calculation results concerned with the analysis of volumetric power at selected points of the welding area (Fig. 18). The selected examples clarified the new approach to electrode displacement control and demonstrated the convergence of the results obtained in the numerical calculations and in the experimental tests.

Figure 15 presents the comparison of the numerical calculation results and the results of the metallographic tests in relation to the analysis of temperature and current density in selected numerical model mesh nodes. Fig. 15(a/c) presents (partly) the welded joint metallographic structure where the connection of the welded materials was obtained. Figure 15a is related to the EFS, whereas Fig. 15c is related to the PFS.

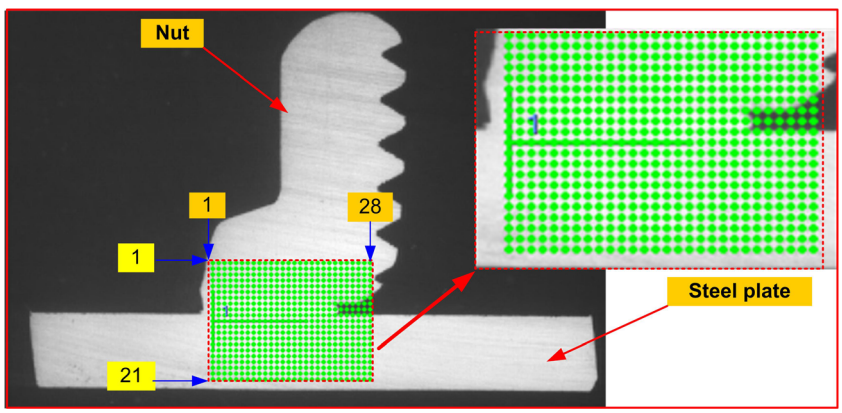

Fig. 13 Arrangement of points in the hardness measurement involving the nut-sheet welded joint

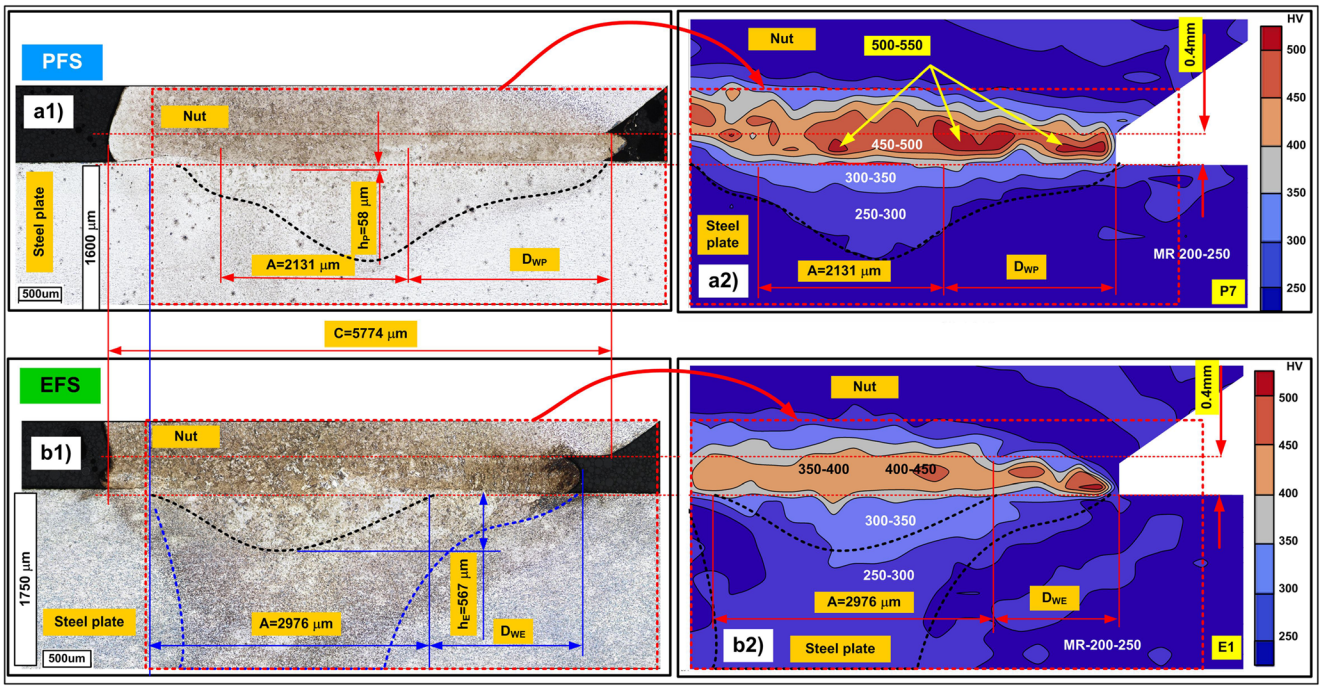

Fig. 14 Metallographic structures of the welded joints in relation to: **a** PFS (P7) and **b** EFS (E1) along with the welding area hardness map

The fragments of the metallographic structures were selected from Figs. 10 to 9 respectively (presenting the entire metallographic image of the joints). The comparative analysis was based on three points arranged geometrically in the sheet, under the nut projection material. The above-named points were numerical model mesh nodes numbered 431, 415 and 403, and located $^1/_6$, $^1/_3$ and ½ mm (Fig. 2c) away from the sheet upper surface, respectively. Figure 15d presents the magnified image related to the temperature courses shown in Fig. 8 (related to both electrode force systems) along with welding current waveforms (as synchronising waveforms). The EFS-related technological tests and metallographic tests (Fig. 14 (b1)) revealed deeper penetration in the sheet (h_E = 567 µm) than that obtained using the PFS (Fig. 14 (a1), h_P = 58 µm). The above-named greater penetration could be attributed to the more favourable distribution of welding power. In Fig. 15b, the aforesaid distribution is presented in the form of EFS-related higher welding current density (Fig. 15a, point C). Appropriately slowed down and controlled electrode force was responsible for lower force, a smaller contact area between welded elements and higher contact resistance, which, in spite of lower current (14.0 kA), enabled the obtainment of higher current density. The maximum values of power density concerned with node No. 403 amounted to 335 and 225 A/mm^2 (Fig. 15b) in relation to the EFS and PFS, respectively. It was important that high current density was obtained at the very beginning of the welding process (first 20 ÷ 30 ms), which led to the melting (and not only to the plasticising) of the projection material from the very beginning. Higher current density led to the generation of higher power of the process performed using the EFS (Fig. 8 (curve 5b)) than that obtained using the PFS (Fig. 8 (curve 2b)), which, in turn, resulted in the obtainment of higher temperature in the aforesaid area.

In selected EFS-related nodes (A-431, B-415 and C-403), temperature exceeded a melting point of 1500 °C. The foregoing was confirmed by the metallographic test results, revealing penetration depth (weld nugget height) h_E = 567 µm. In turn, as regards the PFS, at the same mesh nodes (D-431, E-415 and F-403) the melting point (1500 °C) was not obtained. At a distance of $^1/_6$ mm from the upper surface of the sheet the maximum temperature amounted to 1383 °C. The foregoing was confirmed by the metallographic test results, revealing penetration depth (weld nugget height) h_P = 58 µm. The numerical test results presented in Fig. 15 were entirely consistent with the metallographic test results.

Figure 16 presents the comparison of the metallographic test results with the temperature distribution obtained in the numerical calculations. The dashed line marks the area of the molten material in relation to the metallographic structures obtained using the PFS (Fig. 16 (a1)) and EFS (Fig. 16 (b1)). The figure also contains the temperature distribution images obtained in the numerical calculations (Fig. 16 (a2/b2)). After plotting the contours of the molten material area in relation to the PFS (Fig. 16 (a2)) and EFS (Fig. 16 (b2)), it was possible to observe high similarity in terms of the weld nugget formation as regards the weld width and height.

Figure 17 presents the results of the experimental tests, i.e. the comparison of the characteristic parameters

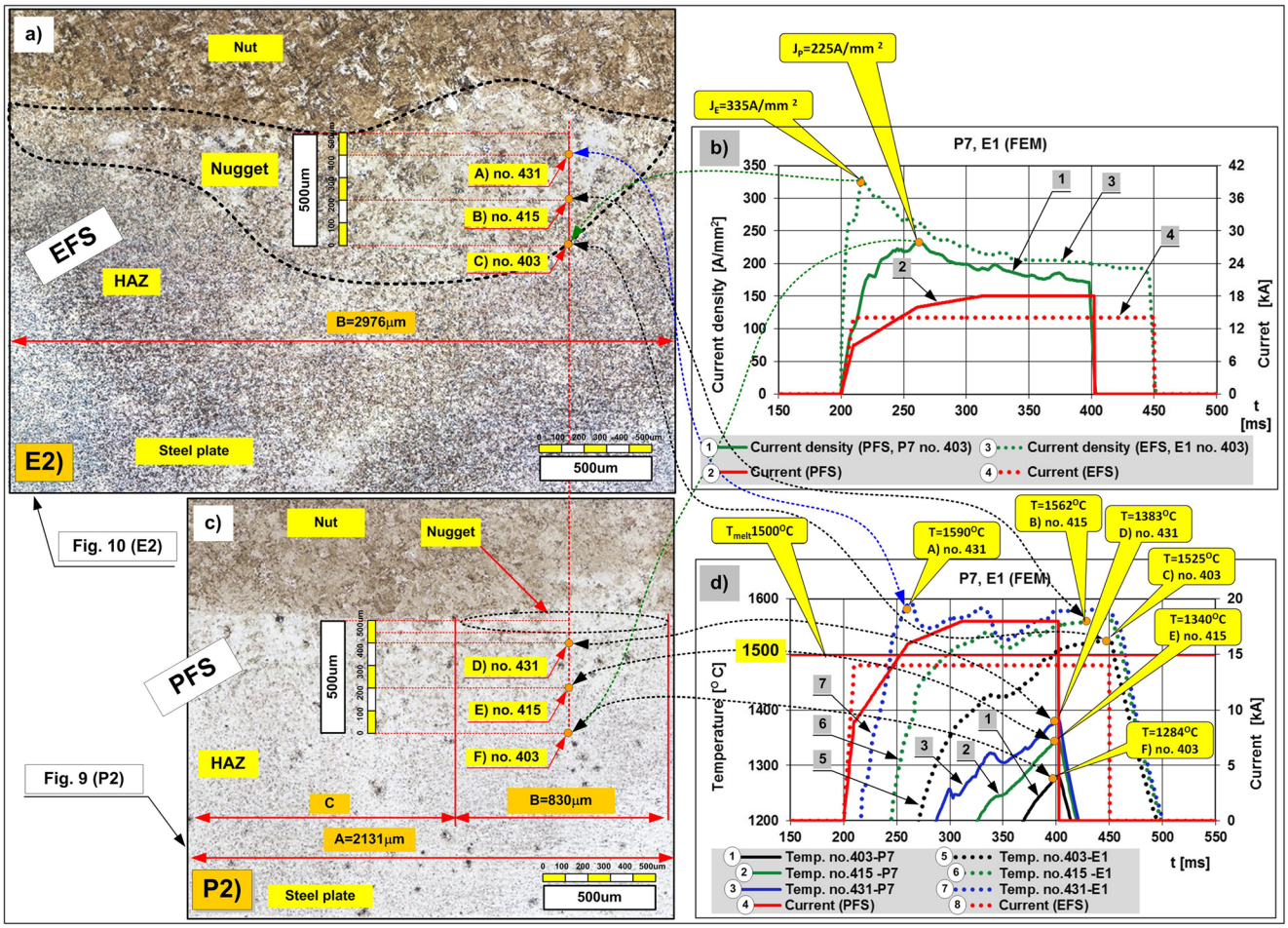

Fig. 15 Comparison of the FEM results and the metallographic test results (temperature, current density) in relation to selected numerical model mesh nodes and metallographic structure (P7 and E1)

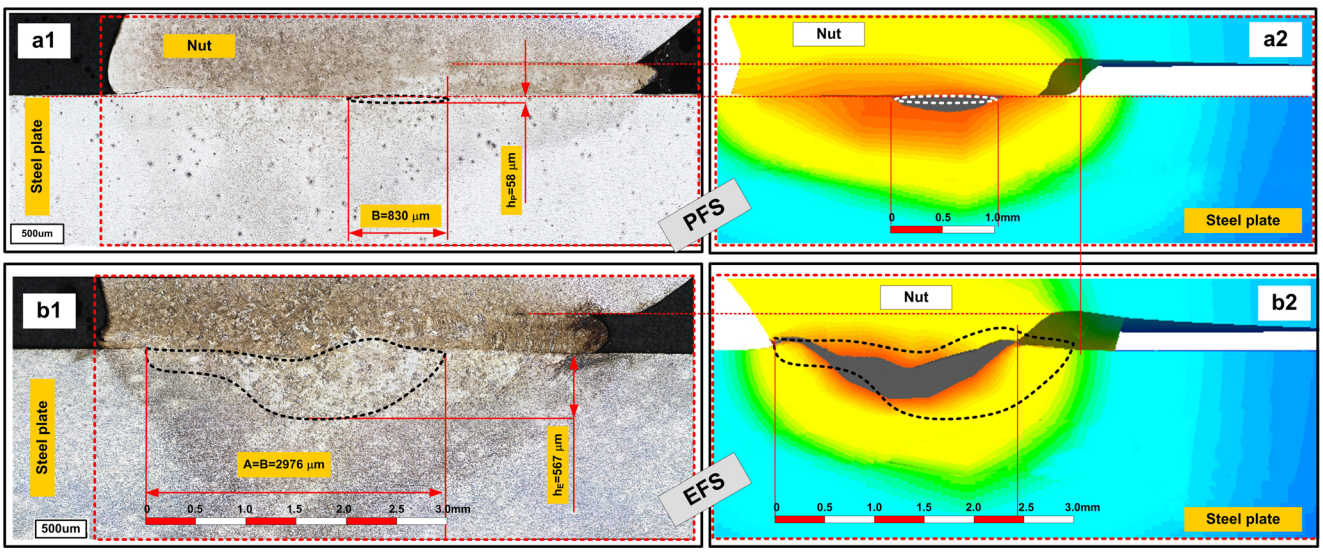

Fig. 16 Comparison of the FEM results and the metallographic test results in relation to temperature distribution at the end of the welding process (P7 and E1)

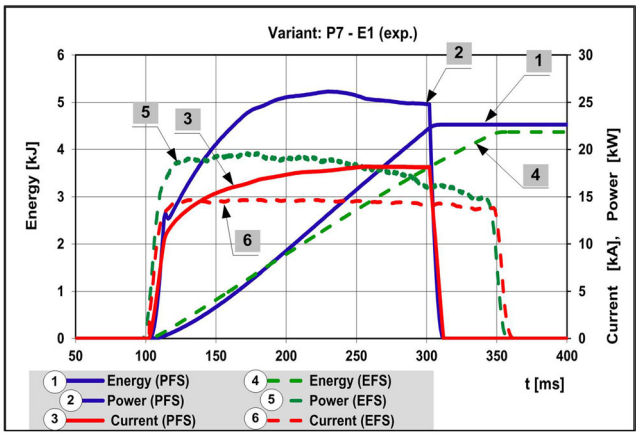

Fig. 17 Experimental comparison of the characteristic parameters (current, momentary power, energy) in relation to the PFS (P7) and EFS (E1)

(current, momentary power, energy) recorded in relation to the technological welding tests and the two analysed electrode force systems (P7 and E1). Figure 18 presents the results of the FEM calculations in relation to volumetric power at selected mesh node No. 636 in the 2D model, located geometrically at the same point as node 403 in the 3D model.

Both figures make it possible to present advantages of the EFS over the PFS. The sequence of events (particularly at the beginning of the flow of current) was the following: (i) contact area between the welded elements was smaller, (ii) current density was higher and (iii) power generated, at the beginning of current flow, in the contact area between the welded elements and in the adjacent area was higher (Fig. 18 (curve 2)). The above-named factors were responsible for the more intense melting of the material in the contact area. The advantages resulting from the control of electrode force were the following: (i) welding current was lower by 28% and (ii) welding process total energy was slightly lower—Fig. 17 (curve 4)).

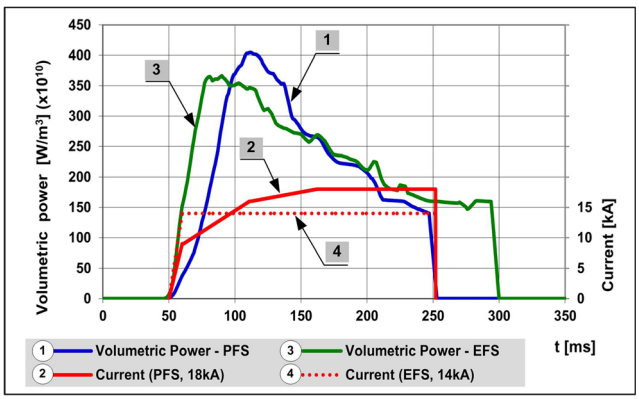

Fig. 18 Volumetric power waveform in relation to (1) PFS (P7) and (2) EFS (E1) (FEM-2D model)

5 Summary

The direction of changes resulting from the use of the EFS and the algorithm of electrode force and displacement control is entirely different from previously adopted approaches. Undertaken activities produced a positive and very desirable effect in the form of more favourable space distribution of welding power, i.e. increased welding power density, particularly in the contact area between elements being welded.

The principal difference between the two electrode force systems is the fact that, in terms of the PFS, (electrode) force was preset and the displacement of electrodes was the result. In turn, as regards the EFS and the new (hybrid) control algorithm, displacement (of electrodes during the flow of current) was preset and the force of electrodes was the result. The foregoing led to the slower displacement of electrodes than that obtained using the PFS. In addition, as regards the EFS, the course of electrode force was more favourable and the value of force was lower. As a result, it was possible to generate higher energy and, consequently, heat in the contact area between elements being welded.

The welding process performed using the EFS involved the use of a lower welding current of 14.0 kA (by 28%) than that used during welding performed using the PFS (18.0 kA). In spite of the foregoing (i) volume of the weld nugget molten material increased more than four times (according to FEM calculations from 4.7 to 21.0 mm^3), (ii) weld area increased more than two times (according to FEM calculations from 24.0 to 53.2 mm^2), (iii) penetration depth increased three times (according to FEM calculations from 0.15 to 0.5 mm) (exp. ten times from 58 to 567 μm), (iv) welding energy was slightly lower (exp. from 4.6 to 4.4 kJ), (v) breaking torque (M_B) increased by 30% (exp. from 220 to 300 Nm) and (vi) more favourable joint hardness distribution was obtained.

The analysis was performed using 2D and 3D numerical models (SORPAS). The calculation results were verified experimentally.

The proposed innovative control of electrode displacement could revolutionise and alter previously existing views on the course of the resistance welding process and significantly affect the development of welding engineering.

Presently, the control of electrode displacement in relation to the EFS during the flow of current is based on a previously defined displacement profile. The profile is a preset parameter and the control system implements this profile without feedback.

Funding information This work was supported by the Polish National Centre for Research and Development (NCBR) under project no. TANGO1/267374/NCBR/2015.

Abbreviations PFS, pneumatic (electrode) force system; EFS, electromechanical (electrode) force system; $\Delta L_{PWE}/\Delta L_{EWE}$, displacement of electrodes at the end of a welding process in relation to PFS and EFS;

$\Delta L_{PCFT}/\Delta L_{ECFT}$, displacement of electrodes during current flow in relation to PFS and EFS; $\Delta L_{PPHRC}/\Delta L_{EPHRC}$, projection height reduction (cold) in relation to PFS and EFS; S_P/S_E, weld area in relation to PFS and EFS; V_P/V_E, weld volume in relation to PFS and EFS; h_P/h_E, penetration depth (weld nugget height) in relation to PFS and EFS; up-slope, current up-slope time; M_B, breaking torque (ISO 898-7); A, weld nugget width (molten material); B, total weld width; D_A, D_T, width of a joint (away from and toward the nut axis) without connection

References

1. Larsson J (2008) Projection welding for nut and bolt attachment. The Fabricator. February 2008. https://www.thefabricator.com/article/shopmanagement/projection-welding-for-nut-and-bolt-attachment. Accessed 14 Apr 2018
2. Lawrence A (2010) Projection welding. Welding Technology Corp. http://www.weldtechcorp.com/welding_concepts/projectionweld.html. Accessed 14 Apr 2018
3. Sun B (2001) Effect of projection height on projection collapse and nugget formation—a finite element study. Supplement to the Welding Journal
4. Mikno Z (2013) Projection welding—process analysis (in Polish). Conference proceeding, Symulacja 2013, Spala, Poland 18–19 Apr 2013, pp. 1–9
5. Zhang H, Senkara J (2011) Resistance welding fundamentals and applications. Taylor & Francis Group, Didcot
6. Zhang X, Chen G, Zhang Y, Lai H (2009) Improvement of resistance spot weldability for dual-phase (DP600) steels using servo gun. J Mater Process Technol 2009:2671–2675
7. Tang H, Hou W, Hu S (2002) Forging force in resistance spot welding. Proc Inst Mech Eng, Part B: J Eng Manuf 216(7)
8. Tang H, Hou W, Hu SJ (2002) Forging force in resistance welding. Proc Inst Mech Eng B J Eng Manuf 216:957–968
9. Gould J (2012) Joining aluminium sheet in the automotive industry—a 30 year history. Welding Journal (Welding Research) vol. 91. January, pp. 23–34
10. Zhang XQ, Chen G, Zhang YS (2008) On-line evaluation of electrode wear by servo gun in resistance spot welding. Int J Adv Manuf Technol 36:681–688
11. Slavick SA (1999) Using Servoguns for automated resistance welding. Weld J 78(7):29–33
12. Sun HT, Lai YS, Shen J (2007) Effect of variable electrode force on weld quality in resistance spot welding. Journal Science and Technology of Welding and Joining 12:718–724
13. Agapiou JS, Perry TA (2013) Resistance mash welding for joining of copper conductors for electric motors. J Manuf Process 15:549–557
14. Zhang XQ, Chen GL, Zhang YS (2008) On line evaluation of electrode wear by servo gun in resistance spot welding. Int Journal Adv Manuf Technol 36:681–688
15. Nachimani C (2017) Techniques for the improvement of carbon steels welds: under the SISF and DIDF welding schemes using pneumatic- and servo-based electrode actuating systems in resistance spot welding. T Int J Adv Manuf Technol 89:3161–3168
16. Mikno Z (2016) Projection welding with pneumatic and Servomechanical electrode operating force systems. Weld J (Welding Research) vol. 95. August, pp. 286-299
17. Mikno Z, Stepien M, Grzesik B (2017) Optimization of resistance welding by using electric servo actuator. Welding in the World Open Access 61:453–462. https://doi.org/10.1007/s40194-017-0437-x
18. SWANTEC. (2015a) SORPAS Software model 2D version 12.0. http://swantec.com/
19. SWANTEC. (2015b) SORPAS Software model 3D version 4.0 x 64. http://swantec.com/
20. SWANTEC. (2015c) User Manual SORPAS. SWANTEC Software and Engineering ApS
21. Nielsen CV, Zhang W, Alves LM, Bay N, Martins PAF (2013) Modelling of thermo-electro-mechanical manufacturing processes—applications in metal forming and resistance welding. Springer Briefs in Applied Sciences and Technology
22. AWS (2018) Welding handbook, 9th edn, vol. 3, welding processes, part 2 chapter 2, projection welding
23. Gould JE (1993) Projection welding. ASM International. ASM handbook, vol. 6. Welding, brazing, and soldering (USA), pp. 230–237, 1993
24. Papkala H (2003) Resistance welding of metals (in polish). KaBe, Krosno
25. SSAB (2018) PN-EN 10149-2:2014-02: hot-rolled flat products of steel with increased yield strength for cold forming
26. Mikno Z, Bartnik Z, Ambroziak A, Pietras A, Mikno M, Niemiec M (2012) Polish patent (P. 220870). Method for projection resistance welding of steel plates with embossed projections
27. Mikno Z, Pietras A, Grzesik B, Stepien M (2017) Polish patent (P.412615). A manner of resistance projection welding in configuration of the cross, mainly for aluminium bars